ARTICLE   **Open Access**

Hybrid optofluidics and three-dimensional manipulation based on hybrid photothermal waveguides

Jiapeng Zheng[1,2], Xiaobo Xing[1,2], Jianxin Yang[2], Kezhang Shi[3] and Sailing He[2,3,4]

Abstract
Despite enormous breakthroughs in lab-on-a-chip techniques, light-driven manipulation faces two long-standing challenges: the ability to achieve both multiform manipulation and tunable manipulation range and the means to avoid potential thermal damage to the targets. By harnessing the optical heating of hybrid photothermal waveguides (HPW), we develop a hybrid optofluidic technique involving buoyancy and thermocapillary convection to achieve fluid transport with controllable modes and tunable strength. Switching of the optofluidic mode from buoyancy to thermocapillary convection, namely, from vertical to horizontal vortices, is employed for three-dimensional manipulation. The strong confinement and torque in the vortices are capable of trapping and rotating/spinning particles at the vortex centers rather than the HPW. Buoyancy convection provides a trapping circle to achieve collective trapping and vertical rotation/spin, while thermocapillary convection offers a trapping lattice to achieve distributed trapping and horizontal rotation/spin. By integrating micro/nanoparticles with various properties and sizes, further investigations of the optofluidic arrangement, mixing, and synthesis will broaden the potential applications of the hybrid optofluidic technique in the fields of lab-on-a-chip, materials science, chemical synthesis and analysis, photonics, and nanoscience.

Introduction

The extraordinary ability of highly efficient non-contact manipulation based on optical systems has stimulated a number of breakthroughs in lab-on-a-chip techniques and research endeavors[1,2]. Keeping pace with the increasingly prevalent development of applications, various requirements for particle manipulation have been presented to accommodate various state-of-the-art microfluidic devices. In view of the current deficiency of light-driven manipulation, there are two fundamental challenges demanding prompt solutions. The first is strong compatibility with many lab-on-a-chip applications, enabling both multiform manipulation and tunable manipulation range. Optical tweezers[3–5] can collectively trap various materials at the center of the laser beams to achieve various forms of manipulation, including transporting[6], binding[7,8], and sorting[9–11]. Plasmonic tweezers provide highly enhanced electromagnetic fields for the distributed trapping of particles into periodic arrays of metal structures[12–14]. However, because only a target in close proximity to the laser illumination can be successfully trapped, these conventional laser trapping techniques consistently suffer from limited manipulation area. To achieve light-driven manipulation with extensive scale, the synergistic integration of optical systems and microfluidic flow has been utilized to control particle movement in a process called optofluidic manipulation[15,16]. Previous works have demonstrated optofluidic flows, including buoyancy convection stimulated by plasmonic

Correspondence: Xiaobo Xing (xingxiaobo@scnu.edu.cn) or Sailing He (sailing@jorcep.org)
[1]MOE Key Laboratory of Laser Life Science & Institute of Laser Life Science, College of Biophotonics, South China Normal University, Guangzhou 510631, China
[2]Centre for Optical and Electromagnetic Research, Guangdong Provincial Key Laboratory of Optical Information Materials and Technology, South China Academy of Advanced Optoelectronics, South China Normal University, Guangzhou 510006, China
Full list of author information is available at the end of the article.

heating[17−21] and thermocapillary flows stimulated by laser-induced microbubbles[22−25]. Despite fast fluid velocity and extensive scaling, photothermally induced fluidic trapping has been simply applied in massive aggregation and long-range transport[17−25]. At present, a comprehensive technique, possessing the synergistic capacities of multiform manipulation and tunable manipulation range, has not been well developed.

The second challenge is potential damage to the target materials. Photothermal heating is unavoidable, and the stimulated heat is highly localized at the laser center, which is commonly the stable position for trapped materials. Especially in plasmonic-based systems[26−28], the effective heating resulting from high field enhancement of plasmonic resonance leads to a vast array of biochemical applications, including photothermal therapy[29], drug delivery[30], phase transition control[31], reversible DNA melting[32], photocatalysis[33], and nanowire growth[34]. Permanent contact with the photothermal resource may possibly give rise to undesirable thermal damage or chemical reactions. In many optical strategies, the obstacle of this accessory effect should be successfully suppressed[35,36], but suppression simultaneously diminishes the efficiency of optical manipulation. In many optofluidic strategies, photothermal heating is a unique excitation, which appears to be a quandary. An "ideal" approach, enabling valid manipulation without contact with the photothermal resource, has not been proposed.

Based on our previous study of particle manipulation[37], which is valid only on a fluid surface (rather than inside the fluid), we develop in this paper an optofluidic system involving buoyancy and thermocapillary convection to achieve controllable fluid motion and multiform manipulation inside the fluid (instead of only on the surface), which can overcome the aforementioned challenges. The three-dimensional thermal transfer of fluid is induced by optical heating of a hybrid photothermal waveguide (HPW), which is motivated by a fiber laser without complex laser-illuminated systems. We both theoretically and experimentally demonstrate the use of hybrid optofluidic flow to selectively control vertical and horizontal vortices. The optofluidic flows are capable of controlling particles in the vortex centers rather than on the HPW, avoiding potential thermal damage to the targets. Compared with laser trapping over a limited area, optofluidic flow is applied to control the suspended particles with adjustable scaling, accompanied by a tunable distance from the HPW. Compared with plasmon-induced thermal trapping functions, the on-demand optofluidic modes exhibit multiform manipulation, including (collective or distributed) trapping and (vertical or horizontal) rotation/spin. Taking advantage of trapping and rotating/spinning in the vortex centers, we develop novel applications for the arrangement of the same components based on

buoyancy convection and self-assembly of materials into stable architectures, such as particle networks and droplet capsules, based on thermocapillary convection.
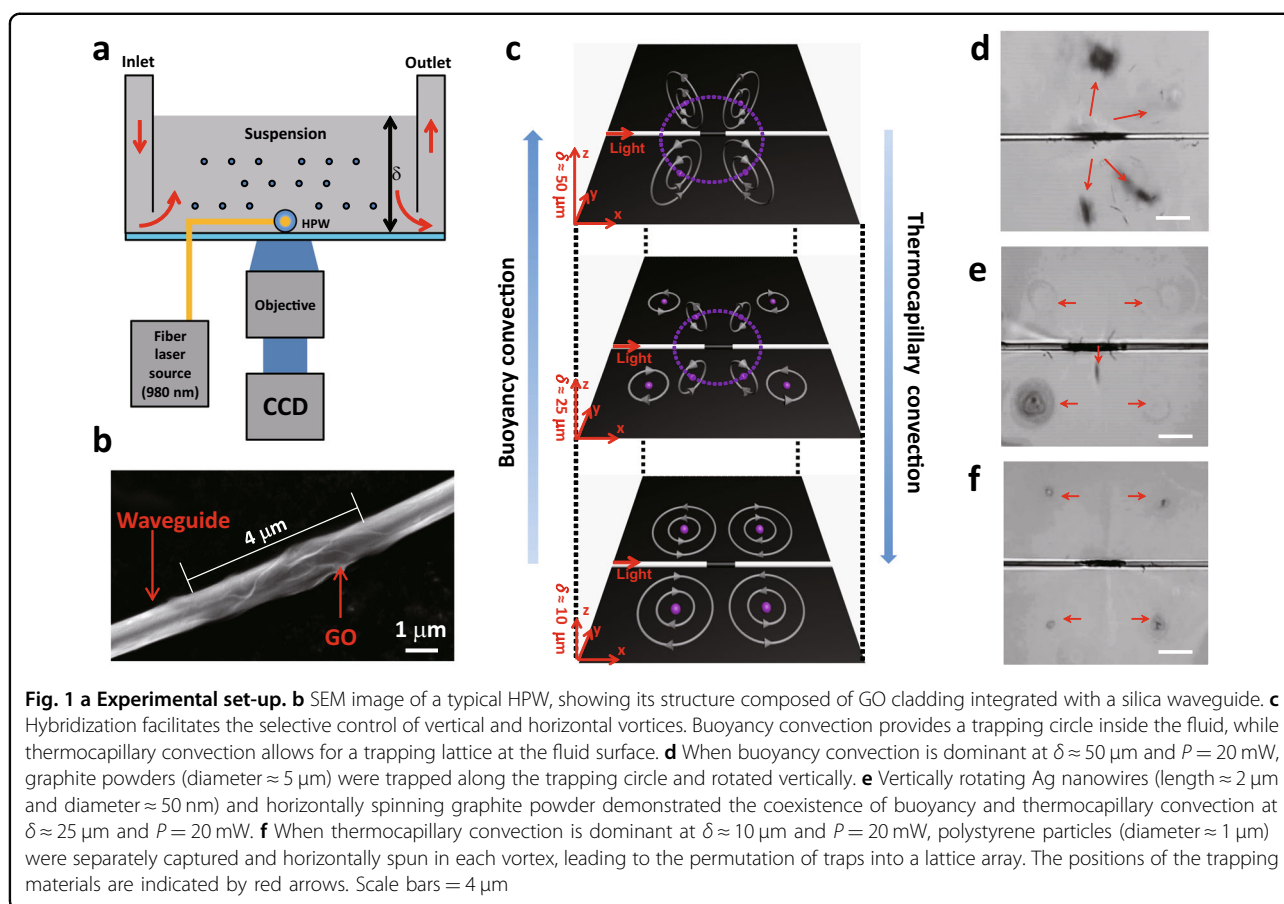
Materials and methods

HPW fabrication

The HPW was fabricated by integrating graphene oxide (GO) with a SiO$_2$ waveguide[22,23]. GO was prepared by the modified Hummers' method. The SiO$_2$ waveguide was drawn by the flame-heated technique. The GO-cladded HPW was fabricated by coating a droplet of GO-ethanol colloid on the waveguide surface, which shrank and automatically formed a thin film as the ethanol evaporated (see Figs. S1−3, Supplementary Information). The length of the GO cladding could be controlled by the droplet length. Experiments showed that after a droplet with volume $V_{droplet} \approx 2$ nL was deposited on the waveguide, the droplet length was fixed at 4 μm. The thickness of the GO cladding could be controlled by the GO concentration C. The quantitative expression between the GO concentration C (units: mg/mL) and the GO-cladding thickness t (units: μm) is $t \approx (0.0046 \cdot C + 0.25)^{1/2} - 0.5$ (see Eq. S4, Supplementary Information). For a GO-ethanol colloid with $C = 25$ mg/mL, we could fabricate a HPW with a length of 4 μm and thickness of 100 nm (see Fig. S2, Supplementary Information). A 980-nm fiber laser with a power of 0−100 mW (PUMP-980-CW, Zhiying, China) was applied. Bubbles were generated when the optical power reached 80 mW, so an optical power of $P = 5$−60 mW was proper for optofluidic convection.

Chip fabrication

As shown in Fig. 1a, the fabricated HPW was deposited on a glass substrate, and the waveguide ends were fixed by paraffin wax. The microfluidic chamber was made from 50-μm thick adhesive tape (area: $S = 1$ cm × 1 cm), and the GO-cladded HPW was located at the center of the bottom of the chamber. Two microfluidic pumps were applied. One was used for the inlet to inject the solvent (volume: V) containing suspended materials, such as Ag nanowires, graphite powder, and polystyrene particles, into the microfluidic chamber. The other was used for the outlet to discharge the fluid (volume: V_{out}) from the microfluidic chamber. A computer-interfaced inverted microscope equipped with a charge coupled device camera (MDX4-T, M-shot, China) was used for observation of the tracing process. A flow situation would destroy the hybrid convection, and thus, the flow velocity and throughput were not considered in the experiments.

Simulation

Two simulation models were applied based on COM-SOL Multiphysics 5.1 (COMSOL Co., Ltd.). The details of the theoretical models, including the geometric model,

Fig. 1 a Experimental set-up. **b** SEM image of a typical HPW, showing its structure composed of GO cladding integrated with a silica waveguide. **c** Hybridization facilitates the selective control of vertical and horizontal vortices. Buoyancy convection provides a trapping circle inside the fluid, while thermocapillary convection allows for a trapping lattice at the fluid surface. **d** When buoyancy convection is dominant at $\delta \approx 50$ μm and $P = 20$ mW, graphite powders (diameter ≈ 5 μm) were trapped along the trapping circle and rotated vertically. **e** Vertically rotating Ag nanowires (length ≈ 2 μm and diameter ≈ 50 nm) and horizontally spinning graphite powder demonstrated the coexistence of buoyancy and thermocapillary convection at $\delta \approx 25$ μm and $P = 20$ mW. **f** When thermocapillary convection is dominant at $\delta \approx 10$ μm and $P = 20$ mW, polystyrene particles (diameter ≈ 1 μm) were separately captured and horizontally spun in each vortex, leading to the permutation of traps into a lattice array. The positions of the trapping materials are indicated by red arrows. Scale bars = 4 μm

material model, and boundary conditions, were described in Fig. S4, Supplementary Information. First was the simulation of the optical heating of the HPW based on an electromagnetic wave model and a heat transfer model, which was used to calculate the temperature T at the front apex of the HPW and the temperature difference ΔT from the front apex to the end of the HPW. The dependences of T and ΔT on the GO-cladding length L and optical power P were studied to demonstrate the optimized HPW morphology to obtain a homogeneous and highest temperature. Second was the thermal-fluidic model simulating the temperature and velocity distribution in the optofluidic flow, based on a heat transfer of fluid model and a laminar flow model. The change in flow thickness δ and HPW temperature T (from the first model) were studied to theoretically show the hybridization and intensity of buoyancy and thermocapillary convection.

Experimental operation for hybrid optofluidic flow

In the experiment, we injected the solvent at $V \approx 5$ μL, and the fluid thickness δ was 50 μm. The fluid in the chamber was discharged with $V_{out} \approx 0.5$ μL each time to decrease the fluid thickness. The resulting fluid thickness was estimated by the volume difference between the

injected and effluent fluid: $\delta = (V - V_{out})/S$. Then, the transition from buoyancy to capillary flow was observed as the change in liquid thickness. Here, the smallest particle diameter was limited to 300 nm. Suspensions of 300-nm polystyrene particles (BaseLine ChromTech Research Centre) were used for tracing the optofluidic flows. A Plan Apo (UPLSAP040X2, 40×, N.A. 0.95) was employed, which had a diffraction limit of approximately 290 nm. M-shot digital imaging software (Image-Pro Plus 6.0) was used for real-time recording of particle trajectories. The recording frame rate was set at approximately 10 Hz. The velocities of the particles were measured by the superposition of the particle trajectories. It was useful to distinguish the optofluidic modes and accurately measure the velocity of tracing particles when buoyancy and thermocapillary convection were dominant.

Experimental setup for optofluidic manipulation

To observe particle movement more clearly, various particles were applied to demonstrate particle manipulation regardless of their shape or surface properties. Suspensions of graphite powders with sizes of 0.5, 1, 2, and 5 μm (XFNANO Advanced Materials Supplier) were used when buoyancy convection was dominant, because the

black color can display more distinct trajectories and positions. Suspensions of polystyrene particles with diameters of 0.5, 1, 2, and 5 μm (BaseLine ChromTech Research Centre) were used when thermocapillary convection was dominant, because their surface flexibility accelerated their interaction. The particle positions and distributions were measured by the Image-Pro Plus 6.0 software package.
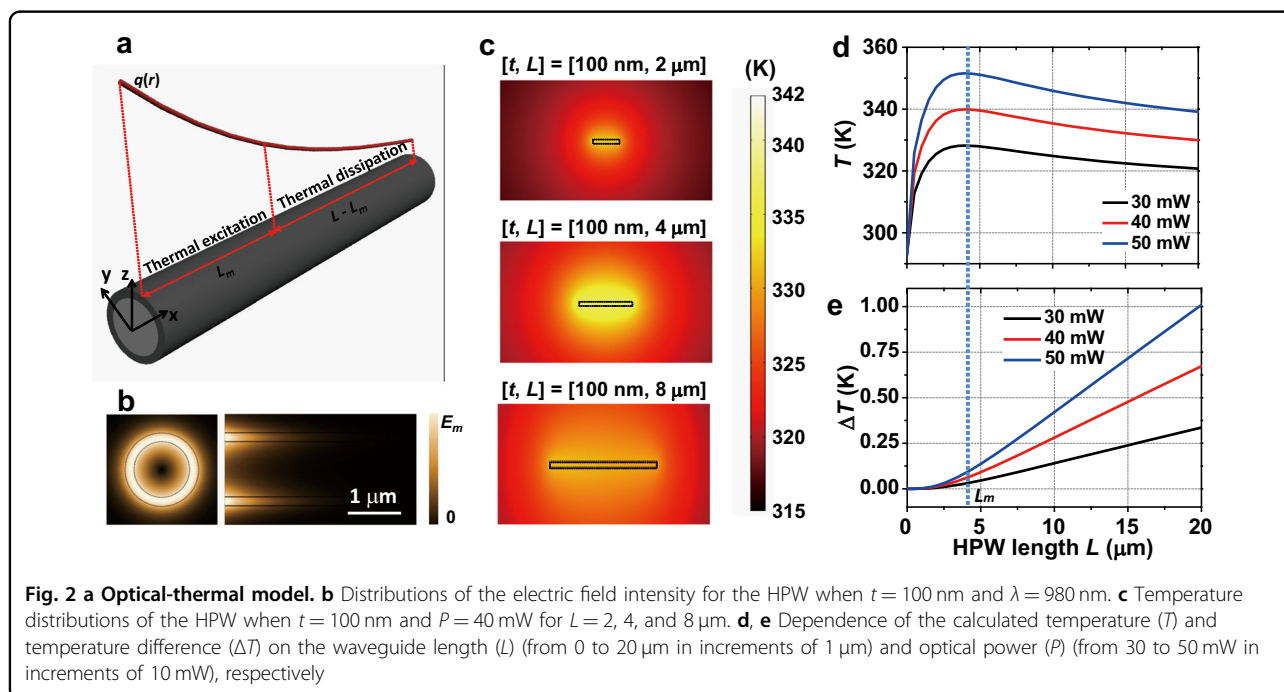
Results and discussion

Construction of the optofluidic system

This novel optofluidic system is synergistically integrated with a photothermal source and a microfluidic device where the fluid surface is in full contact with air, as shown in Fig. 1a. GO is an ideal photothermal material, owing to its strong light confinement, high infrared absorption, and excellent thermal conductivity[38–40], which ensure the stability of the HPW structure and the high efficiency of optical heating. The HPW was fabricated by coating GO on a silica waveguide (Fig. 1b) and served as a photothermal resource, in which the microstructure is capable of yielding strong convection. Activated by a fiber laser at a wavelength of 980 nm, the localized heating of the HPW is three-dimensionally transferred in the fluid, which induces optofluidic flow hybridized by buoyancy convection inside the fluid (vertical vortices) and thermocapillary convection at the fluid surface (horizontal vortices). The alteration of the fluid thickness δ is useful to selectively control the vertical and horizontal vortices, while adjustment of the optical power P is applied to tune the flow velocity and vortex scaling.

Figure 1c shows that the tunable optofluidic modes facilitate three-dimensional optofluidic manipulation. Dominant buoyancy convection can attract and aggregate particles into the trapping circle to achieve collective trapping, while dominant thermocapillary convection enables particles to be separately captured in four independent and equivalent vortices. This trapping can confine the particles in the vortex away from the HPW, preventing the particles from being thermally damaged by the HPW. Figure 1d−f show typical examples of particle confinement without restrictions on the particle material or shape. At large thickness δ ≈ 50 μm, buoyancy convection is dominant, leading to the permutation of irregularly shaped graphite powder along the trapping circle (Fig. 1d). At small thickness δ ≈ 10 μm, thermocapillary convection is dominant, enabling the spheroidal polystyrene particles to be separately captured and horizontally spun in the trapping lattice (Fig. 1f). At the appropriate thickness δ ≈ 25 μm, vertically rotating Ag nanowires and horizontally spinning polystyrene particles were observed simultaneously, demonstrating the superposition of buoyancy and thermocapillary convection (Fig. 1e). The microscopic details of Fig. 1d−f can be viewed in Supplementary Movie 1.

Theoretical simulation for optical heating of the HPW

Figure 2a shows the geometry of the HPW. A 1000 nm-diameter SiO_2 cylinder waveguide coupled with GO cladding with thickness t and length L was immersed in water, forming the HPW. We began the theoretical analyses by estimating the behavior of the electric field

Fig. 2 a Optical-thermal model. b Distributions of the electric field intensity for the HPW when $t = 100$ nm and $λ = 980$ nm. **c** Temperature distributions of the HPW when $t = 100$ nm and $P = 40$ mW for $L = 2$, 4, and 8 μm. **d, e** Dependence of the calculated temperature (T) and temperature difference (ΔT) on the waveguide length (L) (from 0 to 20 μm in increments of 1 μm) and optical power (P) (from 30 to 50 mW in increments of 10 mW), respectively

component $E(r)$ in the HPW, based on the Helmholtz equation:

$$\nabla \times [\nabla \times \mathbf{E}(\mathbf{r})] - k_0^2 \varepsilon(\mathbf{r})\mathbf{E}(\mathbf{r}) = 0, \quad (1)$$

where $k_0 = 2\pi/\lambda$ is the wavenumber corresponding to wavelength λ of the incident light in vacuum. In addition, $\varepsilon(r) = \varepsilon'(r) + i\varepsilon''(r)$ is the position-dependent permittivity with real part $\varepsilon'(r)$ and imaginary part $\varepsilon''(r)$, which are 2.10, $(6.75 + 0.52i)$, and 1.77 for SiO_2, GO[41], and water, respectively, at wavelength of $\lambda = 980$ nm. The optical energy is evanescently coupled into the SiO_2 core and GO cladding and absorbed by the GO cladding. Therefore, the optical energy will exponentially decay along the HPW, leading to non-uniform heat density, as described by[42]

$$q(\mathbf{r}) = k_0 \varepsilon''(\mathbf{r})|\mathbf{E}(\mathbf{r})|^2/2\pi \quad (2)$$

In view of this, the HPW is divided into two parts, as shown in Fig. 2a. The front section is called the "thermal excitation" part, which can be heated sufficiently by integrating the Joule heat along the HPW, as described by[42]

$$Q = \int\int\int q(\mathbf{r})dxdydz. \quad (3)$$

The end section of the HPW is called the "thermal dissipation" part, which is heated based on thermal dissipation[41] from the front section due to its negligible $q(r)$,

$$\nabla \cdot [\kappa(\mathbf{r})\nabla T(\mathbf{r})] = -Q, \quad (4)$$

where $\kappa(r)$ is the thermal conductivity ($\kappa_{GO} = 600$ W m^{-1} K^{-1}, $\kappa_{core} = 27$ W m^{-1} K^{-1}, and $\kappa_{water} = 0.63$ W m^{-1} K^{-1}).

The optimized morphology of the HPW is considered to achieve high efficiency and high sensitivity optical heating, which is the key to yield and control the optofluidic flow. The GO thickness t determines the optical energy distribution in the GO-cladding region (Eq. 1). It is theoretically shown that the optical energy is largely confined to support a tube-like mode for $t = 100$ nm, as shown in Fig. 2b. The GO length L determines the interaction between thermal excitation (Eq. 3) and thermal dissipation (Eq. 4), dominating the temperature distribution in the HPW. Figure 2c shows temperature distributions of the HPW with $t = 100$ nm and $P = 40$ mW for $L = 2$, 4, and 8 µm, exhibiting a visual distinction in optical heating. Figure 2d, e shows the dependence of temperature T at the front apex and temperature difference ΔT between the front and end apex on L and optical power P, respectively. The optimized length L_m was calculated based on Eqs. 1−4. The waveguide with $L < L_m$ achieved the minimal thermal inhomogeneity but exhibited a lower excited temperature due to its insufficient thermal excitation, while the waveguide with $L > L_m$ presents strong thermal inhomogeneity and a lower excited

temperature due to its strong thermal dissipation. For the HPW with $t = 100$ nm, the optimum condition occurs when $L = L_m \approx 4.0$ µm, where both sufficient thermal excitation and negligible thermal dissipation are achieved, resulting in a homogeneous and high temperature along the HPW, despite the change in optical power. For example, as P is increased from 30 to 50 mW, the optimized temperature T_m increases substantially from 328.2 to 351.8 K, while ΔT_m increased insignificantly from 0.05 to 0.1 K.

Theoretical simulation for hybrid optofluidics by the HPW

In the thermal-fluidic models, the temperature distribution $T(r)$ in the surrounding water is governed by the steady-state liquid heat transfer equation[21]:

$$\rho C_p \mathbf{u}(\mathbf{r}) \cdot \nabla T(\mathbf{r}) - \kappa_{water} \nabla^2 T(\mathbf{r}) = 0, \quad (5)$$

where $T(r)$ and $u(r)$ are the fluid temperature and velocity, respectively, $\rho = 10^3$ kg m^{-3} is the density, and $C_p = 4200$ J kg^{-1} K^{-1}) is the specific heat capacity.

The velocity distribution $u(r)$ of thermally induced fluid convection is governed by the steady-state incompressible Navier–Stokes equation[21]:

$$\rho \mathbf{u}(\mathbf{r}) \cdot \nabla \mathbf{u}(\mathbf{r}) - \eta \nabla^2 \mathbf{u}(\mathbf{r}) = F(\mathbf{r}) \, with \nabla \cdot \mathbf{u}(\mathbf{r}) = 0, \quad (6)$$
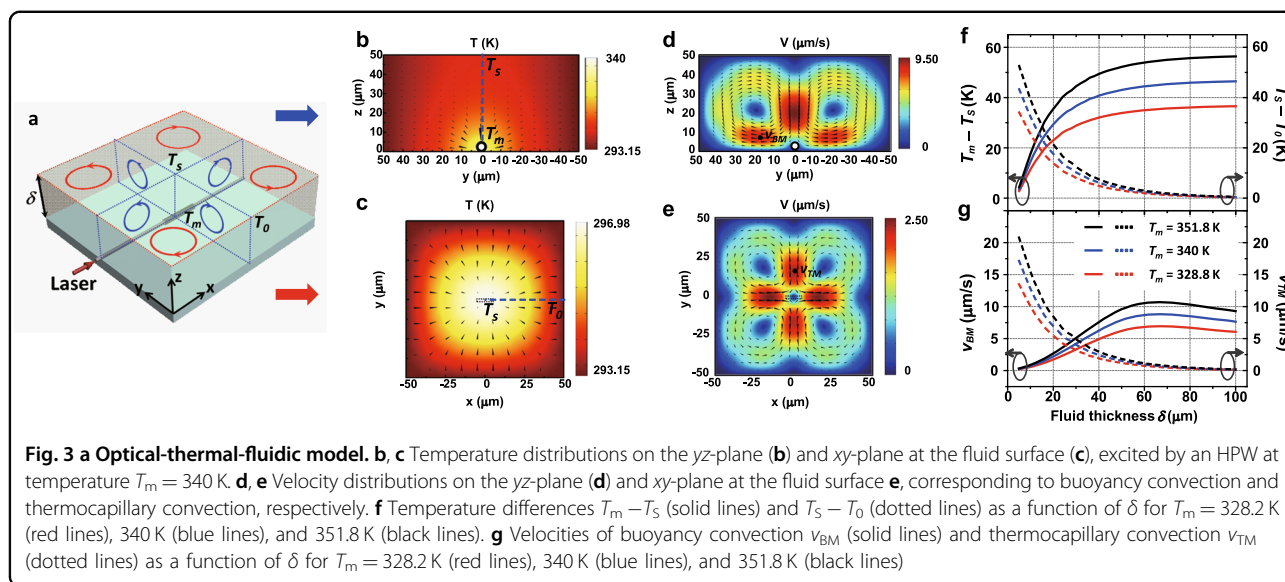
where $\eta = 10^{-3}$ Pa/s denotes the dynamic viscosity. The velocity distribution of the flow $u(r)$ is driven by the $F(r)$ term, representing external forces per unit volume (N m^{-3}), which can be divided into two parts, buoyancy force and surface tension, due to temperature non-uniformity. For most Newtonian liquids, the density and surface tension increase linearly with the decreasing temperature. An imposing temperature gradient correspondingly produces a density gradient inside the fluid and surface tension gradient at the fluid surface, resulting in the external buoyancy force F_B and the surface tension σ_M, respectively:

$$F_B = \rho g \beta_T [T(\mathbf{r}) - T_0] \quad (7)$$
$$\sigma_M = -\sigma_T \cdot \nabla T(\mathbf{r}), \quad (8)$$

where $\rho = 1000$ kg m^{-3} is the fluid density, $g = 9.8$ m s^2 is gravitational acceleration, $\beta_T = 2.07 \times 10^{-4}$ K^{-1} is the thermal expansion coefficient, and $\sigma_T = 1.514 \times 10^{-4}$ N m^{-1} K^{-1} is the temperature coefficient of surface tension. The difference in buoyancy force drives buoyancy convection, while the difference in surface tension drives thermocapillary convection.

The HPW-induced hybrid optofluidics is described as a "superposition" of buoyancy and thermocapillary convection, as shown in Fig. 3a. The temperature distribution of the fluid $T(r)$ in steady state (Eq. 5) induced

Fig. 3 a Optical-thermal-fluidic model. **b**, **c** Temperature distributions on the *yz*-plane (**b**) and *xy*-plane at the fluid surface (**c**), excited by an HPW at temperature $T_m = 340$ K. **d**, **e** Velocity distributions on the *yz*-plane (**d**) and *xy*-plane at the fluid surface **e**, corresponding to buoyancy convection and thermocapillary convection, respectively. **f** Temperature differences $T_m - T_S$ (solid lines) and $T_S - T_0$ (dotted lines) as a function of δ for $T_m = 328.2$ K (red lines), 340 K (blue lines), and 351.8 K (black lines). **g** Velocities of buoyancy convection v_{BM} (solid lines) and thermocapillary convection v_{TM} (dotted lines) as a function of δ for $T_m = 328.2$ K (red lines), 340 K (blue lines), and 351.8 K (black lines)

by the HPW temperature T_m and room temperature T_0, as well as the total force $F(r)$ acting in the fluid including the buoyancy force density F_B inside the fluid (Eq. 7) and surface tension density σ_M at the fluid surface (Eq. 8), synergistically determine the velocity distribution $v(r)$ of buoyancy and thermocapillary convection (Eq. 6). Figure 3b–e show the three-dimensional temperature and velocity distribution of the fluid (100 µm × 100 µm × 50 µm) excited by an HPW at the bottom center with [*t*, L_m, T_m] = [100 nm, 4 µm, 340 K]. From the side view (Fig. 3b) and top view (Fig. 3c), the temperature is dissipated from the bottom center ($T_m = 340$ K) to the surface center ($T_S = 296.98$ K) and from the surface center ($T_S = 296.98$ K) to the surface border ($T_0 = 293.15$ K). Corresponding to the temperature distribution, buoyancy convection is characterized by a kind of three-dimensional toroidal internal flow, vertically flowing toward and away from the HPW (Fig. 3d). Thermocapillary convection is characterized by a type of two-dimensional toroidal surface flow, consisting of four equivalent vortices as a horizontal array (Fig. 3e). Further simulation results of the temperature and velocity distribution for various δ exhibit a more complete picture of the optofluidic flow (see Fig. S5, Supplementary Information).
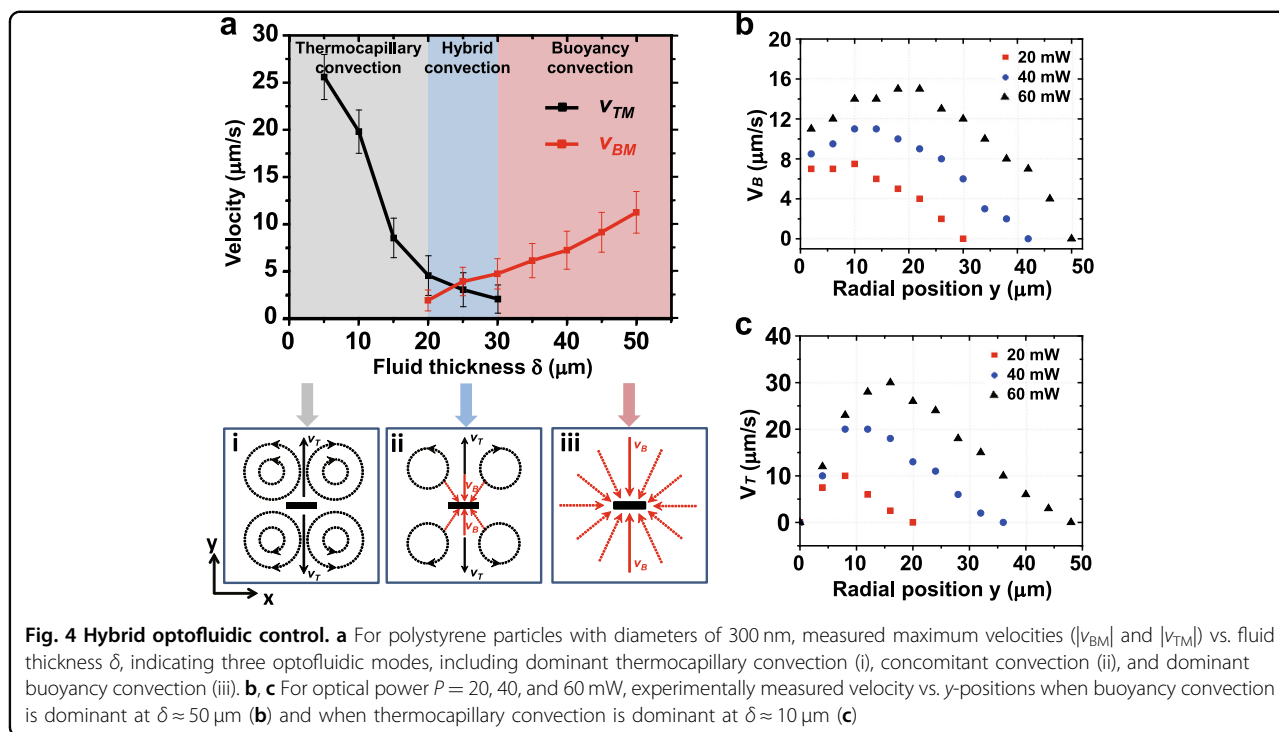
Alterations of δ and T_m are essential to control the hybridization and intensity of the optofluidic flow, respectively. Figure 3f plots the dependence of the temperature differences $T_m - T_S$ and $T_S - T_0$ on δ (from 5 to 100 µm) and T_m (328.2, 340, and 351.8 K). Figure 3g shows the maximum velocity of buoyancy (v_{BM}) and thermocapillary convection (v_{TM}), indicated by the black point in Fig. 3d, e, vs. fluid thickness. It is clear that an increase in δ will lower the temperature gradient at the

liquid surface but increase the temperature gradient inside the liquid, accordingly leading to decaying thermocapillary convection and enhanced buoyancy convection. For example, at $\delta = 10$ µm, the hybrid optofluidic flow supports dominant thermocapillary convection. While at $\delta = 60$ µm, buoyancy convection is dominant. At $\delta = 30$ µm, thermocapillary convection coexists with buoyancy convection. An increase in T_m will increase the temperature gradient inside the liquid and at the fluid surface and finally reinforce buoyancy and thermocapillary convection.

Experimental verification of the hybrid optofluidic flow

To experimentally demonstrate the generation of HPW-induced hybrid flows, we fabricated an HPW with $L \approx 4$ µm and $t \approx 100$ nm by transferring prepared GO onto a SiO$_2$ waveguide with a radius of 500 nm and deposited it on a glass substrate (see Figs. S1–3, Supplementary Information). The temperature of the HPW and the temperature distribution in the surrounding liquid were experimentally demonstrated. We performed direct thermal characterization based on the phase transformation of a paraffin layer under excitation at different optical powers. According to the melted footprint in the paraffin, the HPW temperature could be estimated to be 332−368 K for $P = 30−60$ mW (Fig. S6, Supplementary Information). The flow modes were characterized by the dragged trajectories of the polystyrene particles (diameter = 300 nm) introduced in the chip, and the flow intensity was measured by the particle velocities (Figs. S7−9, Supplementary Information).

We first considered the difference between buoyancy convection and thermocapillary convection. As shown by the microscopic images in Fig. 4a i−iii, buoyancy

Fig. 4 Hybrid optofluidic control. a For polystyrene particles with diameters of 300 nm, measured maximum velocities ($|v_{BM}|$ and $|v_{TM}|$) vs. fluid thickness δ, indicating three optofluidic modes, including dominant thermocapillary convection (i), concomitant convection (ii), and dominant buoyancy convection (iii). **b, c** For optical power $P = 20$, 40, and 60 mW, experimentally measured velocity vs. y-positions when buoyancy convection is dominant at $δ ≈ 50 μm$ (**b**) and when thermocapillary convection is dominant at $δ ≈ 10 μm$ (**c**)

convection could drive the particles toward the HPW by a closely centrosymmetric flow field, while thermocapillary convection kept the particles away from the HPW, forming four vortices. We studied the change in optofluidic modes under an optical power $P = 40$ mW. In Fig. 4a, we selected various particles and measured the distribution of the maximum velocities at different positions. Therefore, the error bars in Fig. 4a indicate the distribution of the measured maximum velocities. The measured maximum velocities of various particles (v_{BM} and v_{TM}) were dependent on the fluid thickness δ, as shown in Fig. 4a. The buoyancy convection began to appear at $δ ≈ 20 μm$, and the thermocapillary convection began to disappear at $δ ≈ 30 μm$. Therefore, three hybrid modes of HPW-induced convection were divided according to δ: dominant thermocapillary convection ($δ ∈ [0, 20] μm$), concomitant convection ($δ ∈ [20, 30] μm$), and dominant buoyancy convection ($δ ∈ [30, 50] μm$). The flow details are contained in Supplementary Movie 2.

For an individual particle, Fig. 4b, c shows the velocities V_T and V_B vs. radius position y under dominant buoyancy convection and thermocapillary convection, respectively, at $P = 20$, 40, and 60 mW. Here, V_T and V_B in Fig. 4b, c represent the value of the particle velocity only. When buoyancy convection was dominant at $P = 40$ mW, particles located at $y ≈ 42 μm$ were accelerated toward the HPW and reached a maximum v_{BM} of 11.3 μm/s at $y ≈ 14$ μm. When thermocapillary convection was dominant, particles located at $y ≈ 36 μm$ were accelerated away from

the HPW and reached a maximum v_{TM} of 19.8 μm/s at $y ≈ 12 μm$.

We further studied the dependence of the optofluidic strength on the optical power. Increasing the optical power was demonstrated to increase the optofluidic strength, which was reflected in two aspects. The first was enlargement of the convection scaling upon increasing the optical power (see Fig. S7, Supplementary Information), because of the expansion of thermal transfer induced by the increasing temperature of the HPW. The second was the increase in the optofluidic velocity (see Fig. 4b, c), originating from the increase in the temperature gradient.

Theoretical analysis for three-dimensional manipulation

Here, we show a new type of three-dimensional optofluidic trapping and rotation/spin in the HPW-induced hybrid optofluidic system. Based on our previous work, the driving mechanism is attributed to the combination of drag force F_D and inertial force F_I in the optofluidic vortices[37], as given by

$$F_D = 3\pi\eta v D \tag{9}$$

$$F_I = Re \times F_D = 3\pi\rho v^2 D L_S, \tag{10}$$

where v denotes the flow velocity, D is the effective diameter of the particle, $Re = \rho v L_S / \eta$ denotes the Reynolds number, and L_S is the size of the optofluidic vortices. The inertial force F_I, directed toward the vortex centers and perpendicular to the flow direction, is exerted to attract

particles into vortex centers. While the drag force F_D, directed along the flow direction, is responsible for circulating particles. The synergy between F_I and F_D drives particles to move spirally toward the vortex centers. Based on the quadratic dependence of F_I on the fluid velocity, F_I is incapable of manipulating particles in the vortex centers, which have minimal flow velocity and correspond to stable trapping positions. Buoyancy convection provides a trapping circle enveloped by the vortex centers inside the fluid, while thermocapillary convection allows for a trapping lattice consisting of four equilibrium positions. All the traps in the vortex centers are controlled by the dominating F_D, leading to vertical rotation under buoyancy convection and horizontal rotation under thermocapillary convection.

Due to the linear dependence of F_I on the particle size D, the rotation modes of particles with different sizes vary in the same vortices. The negligible F_I, combined with the dominating F_D along the flow direction, drives the trapping and rotation of smaller particles (as shown in Fig. 5a). In contrast, larger particles were steadily trapped with spin at the trapping circle or the trapping lattice resulting from the balanced F_I and the predominant F_D (as shown in Fig. 5b).
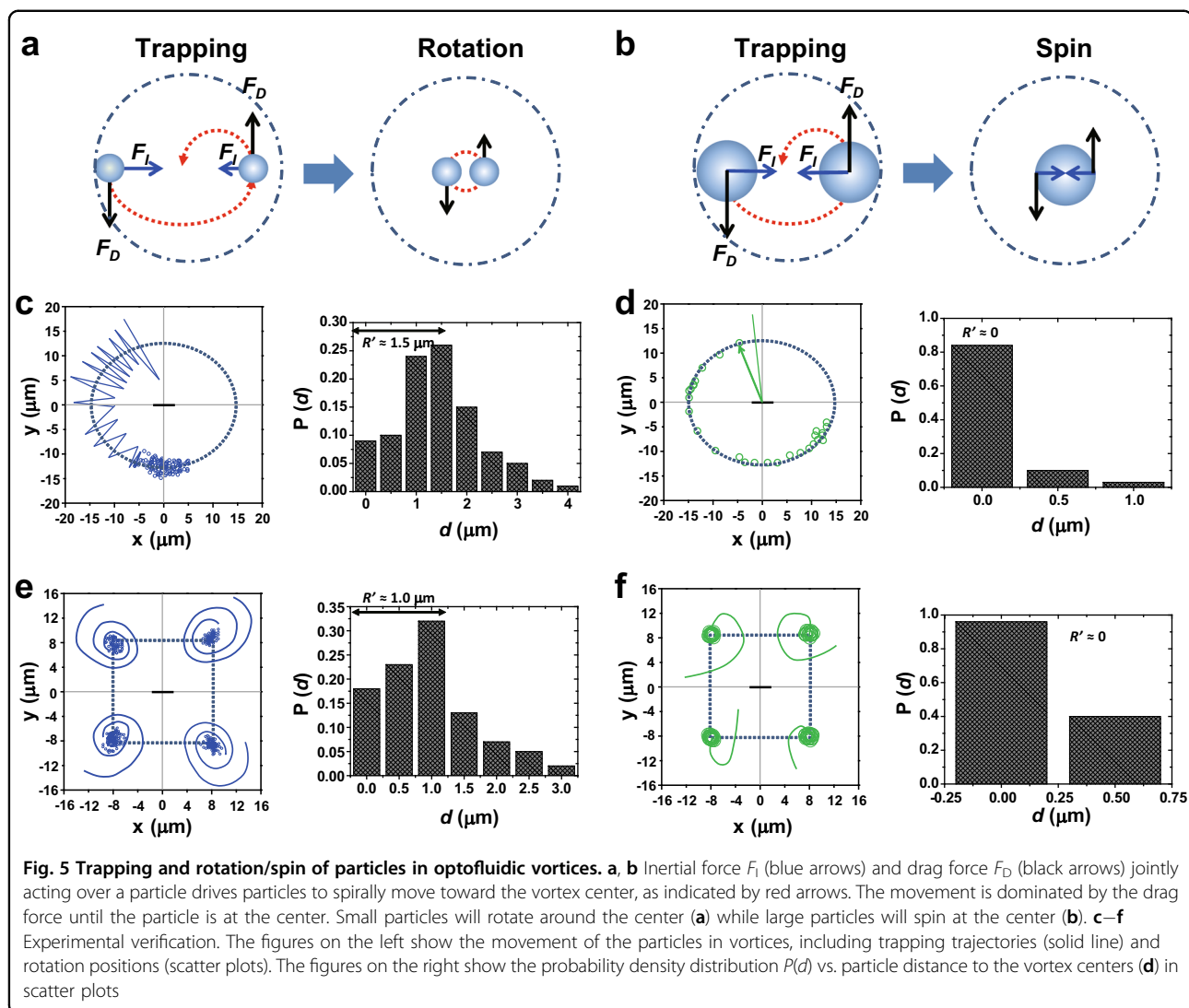
Experimental verification of three-dimensional manipulation

Polystyrene particles with diameters of 1 and 2 μm were used to study trapping modes when buoyancy convection was dominant at $\delta \approx 50$ μm and when thermocapillary convection was dominant at $\delta \approx 10$ μm ($P = 30$ mW), as shown in Fig. 5c–f and Supplementary Movies 3, 4. According to the trapping processes, the recorded movements of particles could be described by two parameters: the trapping transverse trajectories and rotation transverse positions. Under buoyancy convection, theoretically, the trapping trajectories should be a single straight line from the microscopic view (*x*–*y* plane) resulting from F_I and F_D in the *y*–*z* plane. However, buoyancy convection can provide vertical confinement but is incapable of horizontal confinement. Thus, experimentally, the trapping trajectories were always depicted by a polygonal line, and the rotation positions were shown to spread along the trapping circle (Fig. 5c, d). Under thermocapillary convection, which offers horizontal confinement, the trapping trajectories were described by four analogously helical curves, and the rotation positions were scattered around the trapping lattice as a result of F_I and F_D in the *x*–*y* plane (Fig. 5e, f).

Both buoyancy convection and thermocapillary convection showed similar trends in the confinement of particles of various sizes. Owing to the positive dependence of F_I and F_D on the particle size, smaller particles (1 μm) experienced a meandering trajectory around the

trapping circle or trapping lattice, while larger particles (2 μm) were observed to immediately move into the trapping circle or trapping lattice. To study the trapping efficiency and stiffness, the probability density distribution $P(d)$ vs. particle transverse distance to the vortex center (d) was summarized. Shifting of the particles with maximum probability was defined as the effective rotation radius R'. For small particles (1 μm) trapped with rotation, $R' \approx 1.5$ μm under buoyancy convection (Fig. 5c) and $R' \approx 1.0$ μm under thermocapillary convection (Fig. 5e). For larger particles (2 μm), $R' \approx 0$ under both buoyancy convection (Fig. 5d) and thermocapillary convection (Fig. 5f), showing trapping with spin at the vortex centers. In this case, the probability of $P(d)$ (i.e., trapping efficiency) reached a maximum of 82% (Fig. 5d) and 96% (Fig. 5f), respectively. The results demonstrated that decreasing R' decreased particle fluctuation and enhanced particle confinement, meaning that the trapping efficiency reached its maximum when the particles were trapped with spin.

Controlled by the tunable optical power P, varying the scaling of optofluidic flow would lead to a distinct particle trapping status. For different-sized particles, Fig. 6 shows the dependence of trapping, rotation and spin on optical power. Figure 6a, b show the trapping status of the particles, experimentally summarized under dominant buoyancy convection and thermocapillary convection, respectively. The optofluidic flow excited by the under-sized optical power was too weak to realize valid confinement, whereas excessive optical power drove an exaggerated convection for particle trapping with rotation, causing the strong oscillation of particles. Under the appropriate optical power, the trapped particles with continuous spinning were exposed to the stiffest confinement. When buoyancy convection was dominant, the stiffest confinement of particles with different sizes can be achieved at various optical powers. Smaller particles were exposed to the stiffest confinement under lower optical power. Larger particles were subjected to the stiffest confinement over a broader range of optical powers. For example, in Fig. 6a, the stiffest confinement (i.e., trapping with spin) of particles with diameters of 500 nm occurred at $P = 10-15$ mW, whereas that of particles with diameters of 5 μm could be achieved at $P = 20-60$ mW. As shown in Fig. 6c–e, graphite powder with a diameter of 5 μm was trapped and spun vertically when buoyancy convection was dominant ($\delta \approx 50$ μm), and the distance to the HPW increased from 20 to 40 mW. When thermocapillary convection was dominant at $\delta \approx 10$ μm, the stiffest confinement of particles with different sizes can be achieved at the same optical power. For example, when excited at optical powers from 10 to 20 mW (Fig. 6b), particles with diameters of 500 nm to 5 μm can be effectively trapped. As shown in Fig. 6f–h, polystyrene particles with diameters of 1 μm and 500 nm when

Fig. 5 Trapping and rotation/spin of particles in optofluidic vortices. a, b Inertial force F_I (blue arrows) and drag force F_D (black arrows) jointly acting over a particle drives particles to spirally move toward the vortex center, as indicated by red arrows. The movement is dominated by the drag force until the particle is at the center. Small particles will rotate around the center (**a**) while large particles will spin at the center (**b**). **c–f** Experimental verification. The figures on the left show the movement of the particles in vortices, including trapping trajectories (solid line) and rotation positions (scatter plots). The figures on the right show the probability density distribution $P(d)$ vs. particle distance to the vortex centers (**d**) in scatter plots

thermocapillary convection was dominant $(\delta \approx 10\,\mu m)$ were shown to be stiffly trapped and horizontally spun with distances to the HPW of 4 μm at 10 mW, 6 μm at 15 mW, and 8 μm at 20 mW.
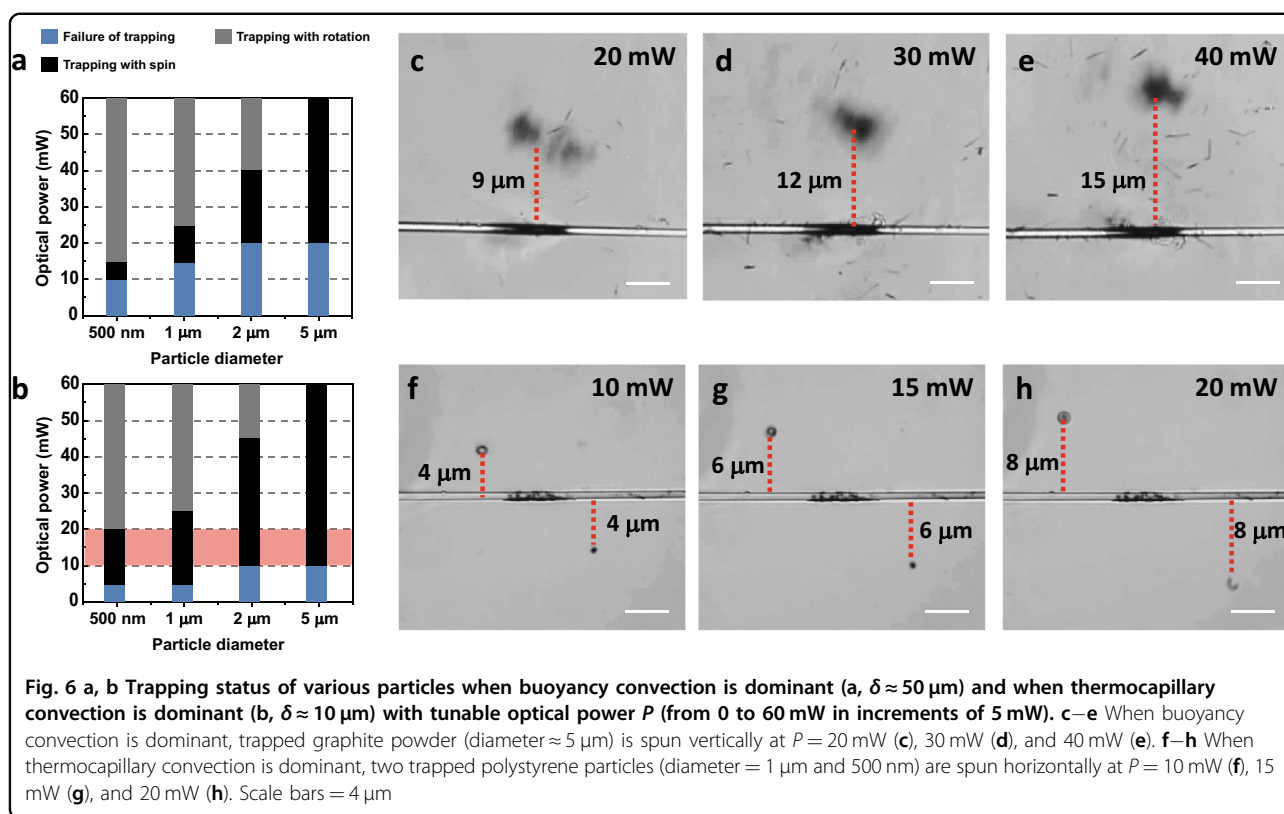
In addition to particle trapping with spin shown (Fig. 6), we provide more examples to identify the dependence of trapping with rotation on different-sized particles in Fig. S10, Supplementary Information. The high optical power drove exaggerated convection, leading to particle trapping with rotation. As the optical power increased, the rotation diameter R' increased, causing strong particle oscillation. It was clear that particles with large R' had strong oscillation and weakened confinement.

Applications for optofluidic arrangement and mixing

In addition to individual manipulation, we further examined real-life applications of the optofluidic system, especially the use of hybrid optofluidic flow for high-throughput particle arrangement and mixing. Control of microscale solid or liquid inclusions is generally a momentous feat in integrated physical detection[43] and chemical reaction[16]. In contrast to other optofluidic systems that demand plasmonic structures[19] or specific surface patterns[44], hybrid optofluidic flow can aggregate particles without limitations on the particles material or the requirement of a substrate, giving a circular arrangement under buoyancy convection and a mixture of square lattices under thermocapillary convection.

By harnessing the dependency of trapping states on the particle size, dominant buoyancy convection can provide a straightforward method for confining particles with appropriate size and arranging them along the trapping circle. Figure 7a, b and Supplementary Movie 5 demonstrate the extraction of 2 μm particles from massive 500 nm particles when buoyancy convection is dominant $(\delta \approx 50\,\mu m$ and $P = 30\,mW)$. The typical escape trajectories

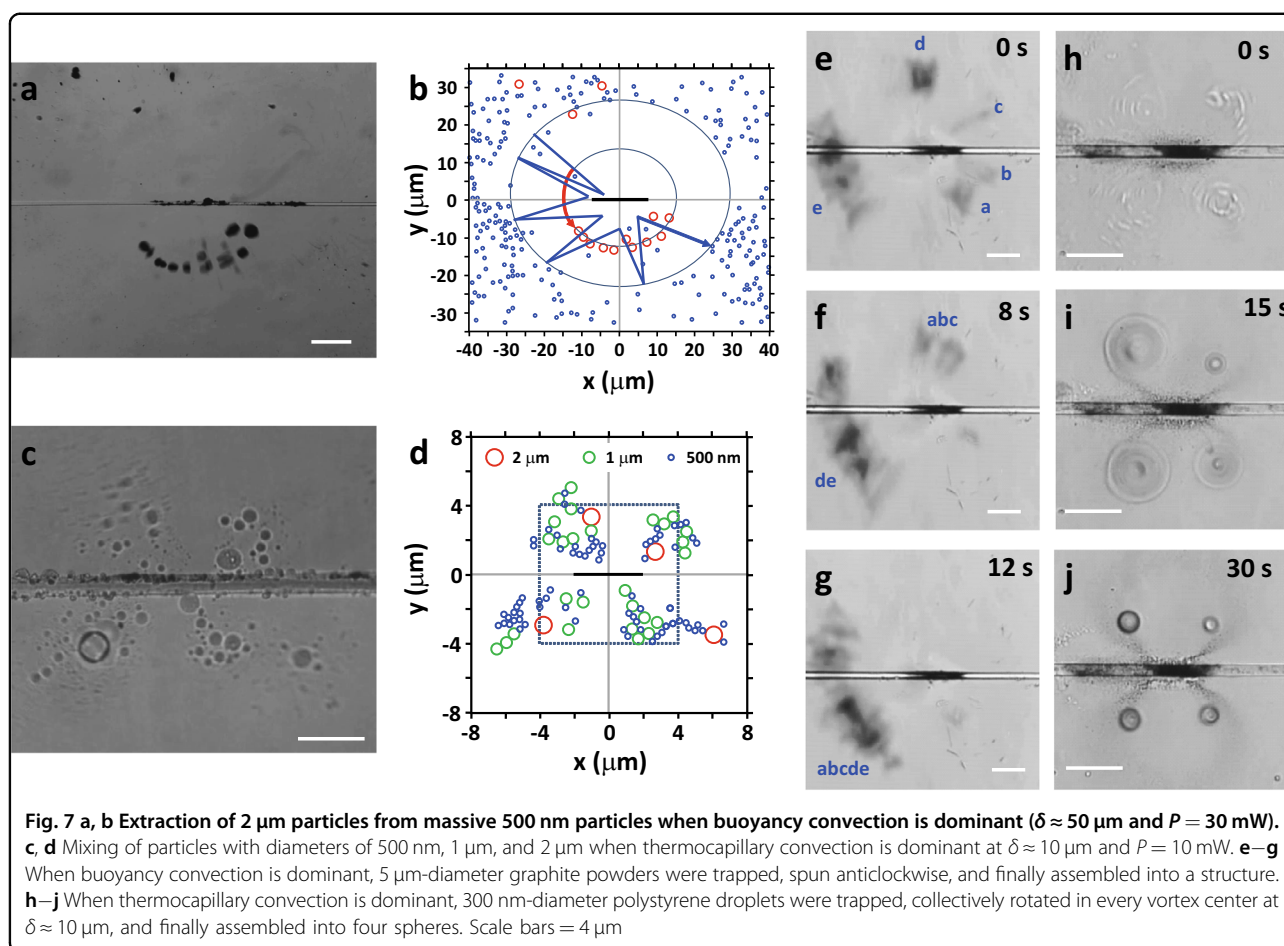**Fig. 6 a, b** Trapping status of various particles when buoyancy convection is dominant (a, $\delta \approx 50\,\mu m$) and when thermocapillary convection is dominant (b, $\delta \approx 10\,\mu m$) with tunable optical power P (from 0 to 60 mW in increments of 5 mW). **c−e** When buoyancy convection is dominant, trapped graphite powder (diameter $\approx 5\,\mu m$) is spun vertically at $P = 20$ mW (**c**), 30 mW (**d**), and 40 mW (**e**). **f−h** When thermocapillary convection is dominant, two trapped polystyrene particles (diameter = 1 μm and 500 nm) are spun horizontally at $P = 10$ mW (**f**), 15 mW (**g**), and 20 mW (**h**). Scale bars = 4 μm

(blue lines) indicate that the 500 nm-diameter particles rotated around the flow boundary with strong oscillation and were rapidly removed, while the typical trapping trajectories (red lines) show that the 2 μm-diameter particles were strongly confined along the trapping circle. Figure 7b shows that most of the 2 μm-diameter particles were arranged along the trapping circle. Some trapped particles could swim along the trapping circle, leading to a self-arranged circular chain. Fig. 7e–g and Supplementary Movie 6 further show that the 5 μm-diameter graphite powders were captured when buoyancy convection was dominant at $\delta \approx 50\,\mu m$ and $P = 20$ mW and then collided with each other, connected end to end, and finally self-arranged in a chain.

The aggregation of desired particles from a mixture can potentially be applied in enhanced sensing platforms. The circular arrangement of 2 μm-diameter fluorescent microspheres from massive 500 nm transparent particles is conducive to enhancing fluorescence detection (see Fig. S11, Supplementary Information). Therefore, it is anticipated that the technique can strengthen the sensing signal based on the aggregation of particles with the same component, providing inspiration for biochemical detection with enhanced sensitivity[43] (for example, by fluorescence detection and Raman spectroscopy).

Dominant thermocapillary convection can trap different-sized particles into the vortex centers with the

stiffest confinement under an optical power of 10–20 mW (Fig. 6b). Figure 7c, d and Supplementary Movie 7 demonstrate the collective aggregation of 500 nm-diameter 1 μm-diameter, and 2-μm-diameter particles when thermocapillary convection is dominant at $\delta \approx 10$ μm and $P = 10$ mW. The distribution of polystyrene particles was observed in the trapping lattice. The collective rotation was accompanied by collisions and squeezing, which strengthened the viscous bonding among the particles. By integrating the strong confinement and torque, different particles can be mixed with constant spins and finally assembled into four particle networks.

The ability to accelerate mass exchange among particles can potentially be used in mesoscopic materials mixing, as reported in previous works[45,46]. Figure S12 (Supplementary Information) shows the transformation process from individual nanoparticles (diameter = 300 nm) to a square lattice of particle clusters ($\delta \approx 10\,\mu m$ and $P = 20$ mW). In the trapping lattice, the nanoparticles were first randomly dispersed, then agglomerated into small particle islands, and finally assembled into large clusters. Fig. 7h−j and Supplementary Movie 8 show the fusion of 300 nm polystyrene droplets into four stable capsules ($\delta \approx 10\,\mu m$ and $P = 10$ mW). In the trapping lattice, the polystyrene droplets were first trapped with a constant spin, subsequently fused into extensive patches (diameter = 1−4

Fig. 7 a, b Extraction of 2 µm particles from massive 500 nm particles when buoyancy convection is dominant ($\delta \approx 50$ µm and $P = 30$ mW). **c, d** Mixing of particles with diameters of 500 nm, 1 µm, and 2 µm when thermocapillary convection is dominant at $\delta \approx 10$ µm and $P = 10$ mW. **e−g** When buoyancy convection is dominant, 5 µm-diameter graphite powders were trapped, spun anticlockwise, and finally assembled into a structure. **h−j** When thermocapillary convection is dominant, 300 nm-diameter polystyrene droplets were trapped, collectively rotated in every vortex center at $\delta \approx 10$ µm, and finally assembled into four spheres. Scale bars = 4 µm

µm), and finally completely folded into capsules with a diameter of 1 µm. The resultant clusters and capsules were formed within a period of 1 min and stably maintained after the light was turned off. Based on the stiff confinement of 0.5−5 µm-diameter particles at optical power $P = 10-20$ mW, optofluidic mixing can progress steadily in the trapping lattice, providing future applications in microfluidic systems, including microreactors, micromixers, and micro-concentrators.

Conclusions

We developed a novel optofluidic technique using both theory and experiment that involves buoyancy convection and thermocapillary convection, which are characterized by vertical vortices and horizontal vortices, respectively. The respective manipulation characteristics of buoyancy and thermocapillary convection were comprehensively analyzed, showing that the former can support a trapping circle for collective trapping and vertical rotation, while the latter can provide a trapping lattice for distributed manipulation and horizontal rotation. The on-demand control of optofluidic modes and strengths can successfully achieve optofluidic manipulation with different

dimensions, various scopes, and multiple functions, as well as without contact with the HPW. This presented approach is highly attractive for a broader range of lab-on-a-chip applications in detection with enhanced sensitivity, microreactors for multicomponent reactions, and material synthesis with abbreviated times.

Author details

[1]MOE Key Laboratory of Laser Life Science & Institute of Laser Life Science, College of Biophotonics, South China Normal University, Guangzhou 510631, China. [2]Centre for Optical and Electromagnetic Research, Guangdong Provincial Key Laboratory of Optical Information Materials and Technology, South China Academy of Advanced Optoelectronics, South China Normal University, Guangzhou 510006, China. [3]State Key Laboratory of Modern Optical Instrumentations, Centre for Optical and Electromagnetic Research, JORCEP, Zhejiang University, Hangzhou 310058, China. [4]Department of Electromagnetic Engineering, JORCEP, School of Electrical Engineering, Royal Institute of Technology, S-100 44 Stockholm, Sweden

Author contributions

J.Z., X.X., and S.H. conceived of the research. J.Z., J.Y., and K.S. performed the experiments, and J.Z. ran the simulations. J.Z. wrote the paper. X.X. and S.H. supervised the research and finalized the manuscript.

Conflict of interest

The authors declare that they have no conflict of interest.

References

1. Grier, D. G. A revolution in optical manipulation. *Nature* **424**, 810–816 (2003).
2. Quidant, R. & Girard, C. Surface-plasmon-based optical manipulation. *Laser Photon. Rev.* **2**, 47–57 (2008).
3. Ashkin, A. Acceleration and trapping of particles by radiation pressure. *Phys. Rev. Lett.* **24**, 156–159 (1970).
4. Paterson, L. et al. Controlled rotation of optically trapped microscopic particles. *Science* **292**, 912–914 (2001).
5. Padgett, M. & Bowman, R. Tweezers with a twist. *Nat. Photon.* **5**, 343–348 (2011).
6. Brzobohatý, O. et al. Experimental demonstration of optical transport, sorting and self-arrangement using a 'tractor beam'. *Nat. Photon.* **7**, 123–127 (2013).
7. Demergis, V. & Florin, E. L. Ultrastrong optical binding of metallic nanoparticles. *Nano Lett.* **12**, 5756–5760 (2012).
8. Dholakia, K. & Zemanek, P. Gripped by light, optical binding. *Rev. Mod. Phys.* **82**, 1767–1791 (2010).
9. MacDonald, M. P., Spalding, G. C. & Dholakia, K. Microfluidic sorting in an optical lattice. *Nature* **426**, 421–424 (2003).
10. Wang, M. M. et al. Microfluidic sorting of mammalian cells by optical force switching. *Nat. Biotechnol.* **23**, 83–87 (2005).
11. Ploschner, M., Cizmar, T., Mazilu, M., Di Falco, A. & Dholakia, K. Bidirectional optical sorting of gold nanoparticles. *Nano. Lett.* **12**, 1923–1927 (2012).
12. Juan, M. L., Righini, M. & Quidant, R. Plasmon nano-optical tweezers. *Nat. Photon.* **5**, 349–356 (2011).
13. Tsai, W. Y., Huang, J. S. & Huang, C. B. Selective trapping or rotation of isotropic dielectric microparticles by optical near field in a plasmonic Archimedes spiral. *Nano. Lett.* **14**, 547–552 (2014).
14. Liu, M., Zentgraf, T., Liu, Y., Bartal, G. & Zhang, X. Light-driven nanoscale plasmonic motors. *Nat. Nanotechnol.* **5**, 570–573 (2010).
15. Psaltis, D., Quake, S. R. & Yang, C. Developing optofluidic technology through the fusion of microfluidics and optics. *Nature* **442**, 381–386 (2006).
16. Fan, X. & White, I. M. Optofluidic microsystems for chemical and biological analysis. *Nat. Photon.* **5**, 591–597 (2011).
17. Williams, S. J., Kumar, A., Green, N. G. & Wereley, S. T. A simple, optically induced electrokinetic method to concentrate and pattern nanoparticles. *Nanoscale* **1**, 133–137 (2009).
18. Ndukaife, J. C. et al. Photothermal heating enabled by plasmonic nanostructures for electrokinetic manipulation and sorting of particles. *ACS Nano* **8**, 9035–9043 (2014).
19. Ndukaife, J. C. et al. Long-range and rapid transport of individual nano-objects by a hybrid electrothermoplasmonic nanotweezer. *Nat. Nanotechnol.* **11**, 53–59 (2015).
20. Roxworthy, B. J., Bhuiya, A. M., Vanka, S. P. & Toussaint, K. C. Understanding and controlling plasmon-induced convection. *Nat. Commun.* **5**, 3173 (2014).
21. Donner, J. S., Baffou, G., McCloskey, D. & Quidant, R. Plasmon-assisted optofluidics. *ACS Nano* **5**, 5457–5462 (2011).
22. Xing, X. et al. Graphene oxide-deposited microfiber, a new photothermal device for various microbubble generation. *Opt. Express* **21**, 31862–31871 (2013).
23. Xing, X. et al. Dynamic behaviors of approximately ellipsoidal microbubbles photothermally generated by a graphene oxide-microheater. *Sci. Rep.* **4**, 6086 (2014).
24. Zheng, Y. et al. Accumulating microparticles and direct-writing micropatterns using a continuous-wave laser-induced vapor bubble. *Lab. Chip.* **11**, 3816–3820 (2011).
25. Fujii, S. et al. Fabrication and placement of a ring structure of nanoparticles by a laser-induced micronanobubble on a gold surface. *Langmuir* **27**, 8605–8610 (2011).
26. Baffou, G. & Quidant, R. Thermo-plasmonics, using metallic nanostructures as nano-sources of heat. *Laser Photonics Rev.* **7**, 171–187 (2013).
27. Coppens, Z. J., Li, W., Walker, D. G. & Valentine, J. G. Probing and controlling photothermal heat generation in plasmonic nanostructures. *Nano Lett.* **13**, 1023–1028 (2013).
28. Schuller, J. A. et al. Plasmonics for extreme light concentration and manipulation. *Nat. Mater.* **9**, 193–204 (2010).
29. Lim, D. K. et al. Enhanced photothermal effect of plasmonic nanoparticles coated with reduced graphene oxide. *Nano Lett.* **13**, 4075–4079 (2013).
30. You, J., Zhang, G. D. & Li, C. Exceptionally high payload of doxorubicin in hollow gold nanospheres for near-infrared light-triggered drug release. *ACS Nano* **4**, 1033–1041 (2010).
31. Urban, A. S. et al. Controlled nanometric phase transitions of phospholipid membranes by plasmonic heating of single gold nanoparticles. *Nano Lett.* **9**, 2903–2908 (2009).
32. Reismann, M., Bretschneider, J. C., von Plessen, G. & Simon, U. Reversible photothermal melting of DNA in DNA-gold-nanoparticle networks. *Small* **4**, 607–610 (2008).
33. Gan, Z. X. et al. Photothermal contribution to enhanced photocatalytic performance of graphene-based nanocomposites. *ACS Nano* **8**, 9304–9310 (2014).
34. Cao, L. Y., Barsic, D. N., Guichard, A. R. & Brongersma, M. L. Plasmon-assisted local temperature control to pattern individual semiconductor nanowires and carbon nanotubes. *Nano. Lett.* **7**, 3523–3527 (2007).
35. Roxworthy, B. J. et al. Application of plasmonic bowtie nanoantenna arrays for optical trapping, stacking, and sorting. *Nano Lett.* **12**, 796–801 (2012).
36. Wang, K., Schonbrun, E., Steinvurzel, P. & Crozier, K. B. Trapping and rotating nanoparticles using a plasmonic nano-tweezer with an integrated heat sink. *Nat. Commun.* **2**, 469 (2011).
37. Zheng, J. P., Xing, X. B., Evans, J. & He, S. L. Optofluidic vortex arrays generated by graphene oxide for tweezers; motors and self-assembly. *NPG Asia Mater.* **8**, e257 (2016).
38. Li, M., Yang, X., Ren, J., Qu, K. & Qu, X. Phototherapy, using graphene oxide high near-infrared absorbance for photothermal treatment of alzheimer's disease. *Adv. Mater.* **24**, 1621–1621 (2012).
39. Zhu, Y. et al. Graphene and graphene oxide, synthesis, properties, and applications. *Adv. Mater.* **22**, 3906–3924 (2010).
40. Acik, M. et al. Unusual infrared-absorption mechanism in thermally reduced graphene oxide. *Nat. Mater.* **9**, 840–845 (2010).
41. Jung, I. et al. Characterization of thermally reduced graphene oxide by imaging ellipsometry. *J. Phys. Chem. C.* **112**, 8499–8506 (2008).
42. Baffou, G., Quidant, R. & de Abajo, F. J. G. Nanoscale control of optical heating in complex plasmonic systems. *ACS Nano* **4**, 709–716 (2010).
43. Patra, P. P., Chikkaraddy, R., Tripathi, R. P., Dasgupta, A. & Kumar, G. P. Plasmofluidic single-molecule surface-enhanced Raman scattering from dynamic assembly of plasmonic nanoparticles. *Nat. Commun.* **5**, 4357 (2014).
44. Hernàndez-Navarro, S., Tierno, P., Farrera, J. A., Ignés-Mullol, J. & Sagués, F. Reconfigurable swarms of nematic colloids controlled by photoactivated surface patterns. *Angew. Chem.* **126**, 10872–10876 (2014).
45. Milak, S., Medlicott, N. & Tucker, L. G. Solid lipid microparticles containing loratadine prepared using a micromixer. *J. Microencapsul.* **23**, 823–831 (2006).
46. Huang, S. H., Wang, S. K., Khoo, H. S. & Tseng, F. G. AC electroosmotic generated in-plane microvortices for stationary or continuous fluid mixing. *Sens. Actuators B Chem.* **125**, 326–336 (2007).